An ultra-rapid acoustic micromixer for synthesis of organic nanoparticles†

M. Reza Rasouli[a] and Maryam Tabrizian iD *[ab]

Mixing is a crucial step in many chemical analyses and synthesis processes, particularly in nanoparticle formation, where it determines the nucleation rate, homogeneity, and physicochemical characteristics of the products. In this study, we propose an energy-efficient acoustic platform based on boundary-driven acoustic streaming, which provides the rapid mixing required to control nanoprecipitation. The device encompasses oscillatory bubbles and sharp edges in the microchannel to transform the acoustic energy into vigorous vortical fluid motions. The combination of bubbles and sharp edges at their immediate proximity induced substantially stronger acoustic microstreams than the simple superposition of their effects. The device could effectively homogenize DI water and fluorescein within a mixing length of 25.2 μm up to a flow rate of 116 μL min^{-1} at a driving voltage of 40 V$_{pp}$, corresponding to a mixing time of 0.8 ms. This rapid mixing was employed to mitigate some complexities in nanoparticle synthesis, namely controlling nanoprecipitation and size, batch to batch variation, synthesis throughput, and clogging. Both polymeric nanoparticles and liposomes were synthesized in this platform and showed a smaller effective size and narrower size distribution in comparison to those obtained by a hydrodynamic flow focusing method. Through changing the mixing time, the effective size of the nanoparticles could be fine-tuned for both polymeric nanoparticles and liposomes. The rapid mixing and strong vortices prevent aggregation of nanoparticles, leading to a substantially higher throughput of liposomes in comparison with that by the hydrodynamic flow focusing method. The straightforward fabrication process of the system coupled with low power consumption, high-controllability, and rapid mixing time renders this mixer a practical platform for a myriad of nano and biotechnological applications.

Introduction

Nanoparticles are the focus of numerous biomedical research studies for developing novel diagnostic assays, enhancing targeted drug delivery, and improving imaging capabilities.[1] The synthesis process of nanoparticles (NPs) directly determines their characteristics such as composition, size, stability, and size distribution.[2–4] To deliver the full potential of nanoconstructs and regulate their behavior in biological environments such as biocompatibility, biodistribution, interaction with the immune system, and therapeutic efficiency, it is imperative to develop highly-controllable and precise methods for their synthesis.[2,3] Nanoprecipitation (also called the solvent displacement method) is the most widely employed bottom-up nanoparticle synthesis method due to its rapidity, simplicity, and reproducibility.[5,6] The confined

and hence, controllable domain of microfluidic platforms lays the foundation to outperform conventional nanoparticle synthesis methods in achieving a homogeneous nucleation environment, which is the key step for the nanoprecipitation of consistent and uniform nanoparticles.[3] To ensure this homogeneity, rapid mixing should be accomplished in a time span shorter than the aggregation time of precursors (usually in the order of 10 milliseconds).[2,3,7] However, the common laminar flow regimes in microfluidic platforms limit the mass transfer across the channel to a slow diffusion process.[8] Various mixing strategies have been developed to address this so-called 'microfluidic mixing challenge'. In passive micromixers (such as hydrodynamic flow focusing (HFF) mixers,[9,10] chaotic mixers,[11] and curved-channel mixers[12]), the channels are engineered to adjust the flow field configuration with the aim of shortening the diffusion length and thereby, the mixing time.[13] Passive mixers, especially HFF mixers, are widely used for nanoparticle synthesis and have shown superior size control and distribution over conventional methods.[3,14,15] However, clogging, dilution, and limited mixing performance can restrict their functionality.[16] In contrast, active mixers use an external source of energy

[a] Biomedical Engineering Department-Faculty of Medicine, McGill University, Montreal, Quebec H3A 2B4, Canada. E-mail: Maryam.Tabrizian@McGill.ca
[b] Faculty of Dentistry, McGill University, Montreal, Quebec H3A 2B4, Canada
† Electronic supplementary information (ESI) available: Fig. S1–S8 (S1.PDF) and Videos S2–S8. See DOI: 10.1039/c9lc00637k

such as electrical, magnetic or acoustic energy and generally present a higher mixing efficiency. Acoustic micromixers offer high mixing efficiency while remaining non-invasive and safe to operate in the proximity of biological and chemical samples. These features coupled with the obviation of requisites such as magnetic particles or conductive fluid medium advance acoustic mixers as versatile devices for biochemical applications.[17]

Acoustic-driven micromixers employ bulk acoustic waves (BAWs),[18] surface acoustic waves (SAWs),[19] and acoustically vibrating microstructures to transfer acoustic energy into the fluid medium and induce mixing. Among the latter, oscillatory sharp edges[20] and bubbles[21] have shown advantage in mixing due to their strong localized microstreams, low power consumption,[22] and facile and inexpensive manufacturing procedure as they do not require interdigitated electrode deposition or expensive piezoelectric substrates. When exposed to an acoustic field, the sharp edges or bubble interfaces function as vibrating boundaries in response to pressure fluctuations of acoustic waves and induce a secondary bulk fluid motion known as acoustic microstreams.[23] Liu *et al.*[24] used acoustically excited bubbles for inducing microvortices and accelerating mixing to a time span of seconds. To stabilize the air bubbles in microchannels, Ahmed *et al.*[25] embedded horseshoe structures that trap bubbles upon passage of fluid in the channel. The bubble-based mechanism was applied for DNA hybridization,[26] enzyme reaction analysis,[27] cell separation,[28] and bacterial aggregation.[29] Similarly, oscillatory sharp edges are shown to generate microstreams using the boundary-driven mechanism with a reportedly comparable performance to that of the bubbles.[30] Huang *et al.*[31] used sharp edges to reduce the mixing time as low as 180 ms. They showed that the intensity of microstreams dramatically increases as the angle of the tip sharpens while the height of the edges can also be influential. Leibacher *et al.*[20] employed acoustically agitated sharp edges to trap cells and particles in a microfluidic channel.

In this study, we demonstrated that acoustic microstreaming could be considerably reinforced by integrating sharp edges and bubbles together in the design of a microfluidic platform to enhance the speed and homogeneity of the mixing. The essence of the design is to magnify the amplitude of vibration in the oscillatory structures by exciting sharp edges and bubbles synchronously. The acoustic streaming intensity and mixing capability of oscillatory bubbles, sharp edges, and the proposed combined unit were compared by measuring their mixing efficiency. To demonstrate the functionality and versatility of the device and introduce a proof of concept application for acoustic micromixers, two types of organic nanoparticles, polymeric (PLGA-PEG) nanoparticles and nanoliposomes, were synthesized. The high controllability of flow streams in the platform was exploited to modulate the size of both nanoparticle types by simply altering the mixing time and to prevent clogging in the channel.

Mixing concept and mechanism

In boundary-driven acoustic streaming, the tangential velocity of the fluid is essentially zero on solid surfaces due to a no-slip boundary condition and rapidly reaches the free-field value within a thin domain characterized by thickness $\delta_v = \sqrt{2\nu/\omega}$ where ω represents the angular frequency of the acoustic wave.[32,33] This steep velocity gradient results in a substantial variation in the momentum of the acoustic wave which subsequently produces significant Reynolds stress forces,[34] leading to strong vortices known as Rayleigh streaming.[35] For a simplified boundary layer condition, the magnitude of the steady streaming velocity is proportional to the square of the oscillatory interface velocity:[28]

$$\mathbf{V_s} \propto \mathbf{V_h}^2/\omega \tag{1}$$

in which $\mathbf{V_s}$ is the streaming velocity and equals the time-average of the second-order velocity field and $\mathbf{V_h}$ is the velocity of the oscillatory interface which can be calculated by:

$$\mathbf{V_h} \sim d\omega \tag{2}$$

Substituting eqn (2) into eqn (1):

$$\mathbf{V_s} \propto d^2\omega \tag{3}$$

where d is the displacement amplitude of the interface. Therefore, the vibration displacement amplitude is the most influential factor in microstream strength due to its squared relationship with the speed of streaming.[36,37]

Bubbles

In response to the local pressure variation of acoustic waves, bubbles in liquid show two modes of displacement: volumetric (radial) oscillation and translational oscillation.[21,38] The compressibility of the gas in a bubble permits the interface to expand and contract by five percent of its initial radius which leads to high-amplitude volume pulsations.[22,39] This large volume pulsation enables the bubble to perform as a secondary acoustic transmitter which locally intensifies the sound field.[40] These phenomena contribute to multiple orders of magnitude stronger microstreams in the immediate proximity of pulsatile bubbles.[38]

Sharp edges

Oscillatory sharp edges form large Reynolds body force and 100-times stronger microstreams compared to their non-sharp analogs.[41] Considering the sharp edge structure as a cantilever, it is assumed that the lower flexural rigidity at its tip yields higher displacement in each stroke and as a result, generates stronger microstreams.[31] However, there is another explanation that also recognizes the centrifugal forces of oscillatory fluids around sharp edges.[41]

On the hypotheses that the integration of the two above-mentioned mechanisms yields mutual enhancement and amplification of the acoustic effects, we developed a microfluidic device with a geometry that incorporates both features, herein referred to as the 'combined unit'. Fig. 1A–C show the design of the microfluidic platform. The length, width, and depth of the channel are 1.2 cm, 600 μm, and 100 μm, respectively. The height of the sharp edges is set at 250 μm and the tip angle of the edges at 15°, as it has been shown to be the optimum angle for microstreaming.[31] The sharp edges are slanted with a sequestered volume between every two of them where air bubbles can be confined upon the passage of fluids, due to low surface tension. The combined units are positioned on the upper side and lower side asymmetrically. As such, the acoustic vortices traverse the fluid interface and transport mass between two fields.

Materials and methods

Materials

A negative photoresist (SU-8, 2050) was purchased from MicroChem Corp., USA. Polydimethylsiloxane (PDMS) was obtained from Dow Corning Corp., Canada. PTFE tubes (RK-06407-41) were from Cole-Parmer Inc., Canada. Analytical grade acetonitrile, fluorescein, and trichloro (1*H*,1*H*,2*H*,2*H*-perfluorooctyl)silane were ordered from Sigma-Aldrich, Canada. 1 mL Hamilton glass syringes were purchased from Fisher Scientific, Canada. Three models of piezoelectric transducers: model 273-073 from RadioShack Corp. USA, model SMBA4510T05M from STEINER & MARTINS INC, USA

and model PB4NB2W from Thorlabs Ltd., USA were purchased. Fluorescent polystyrene particles (PSF-002UM) were purchased from Magsphere, USA. Methoxy poly(ethylene glycol)-*b*-poly(lactide-*co*-glycolide) (mPEG-PLGA) with MWs of ≈5000 Da : 30 000 Da were purchased from Poly-SciTech, USA. 1,2-Dipalmitoyl-*sn*-glycero-3-phosphocholine (DPPC) was ordered from Avanti Polar Lipids Inc. (Alabaster, AL, USA). Parylene-C dimers were obtained from Specialty Coating Systems, USA.

Device fabrication and experimental setup

The device was fabricated through standard photolithography, followed by single-layer soft lithography. The negative photoresist (SU-8, 2050) was spin-coated on a silicon wafer, as per the manufacturer's protocol, to fabricate the master of 100 micron thickness. PDMS was poured on the silanized master to replicate the pattern of the channels and microstructures by soft lithography. The patterned PDMS was bonded onto a glass substrate by plasma surface treatment. A piezoelectric transducer was then mounted on the glass substrate along the side of the PDMS microchannels to complete the assembly of the chip. The devices were then treated with a Parylene coating step. The deposition was conducted using an SCS Labcoter 2 PDS 2010 (Specialty Coating Systems, USA) with 2 grams of Parylene-C dimers which correspond to a coating thickness of 1 μm. Harmonic electrical signals were initiated using a function generator (AFG3011C, Tektronix, USA) which also governed the signal's frequency and waveform. The function generator was then connected to an amplifier (25A250A, Amplifier Research, USA) to regulate the
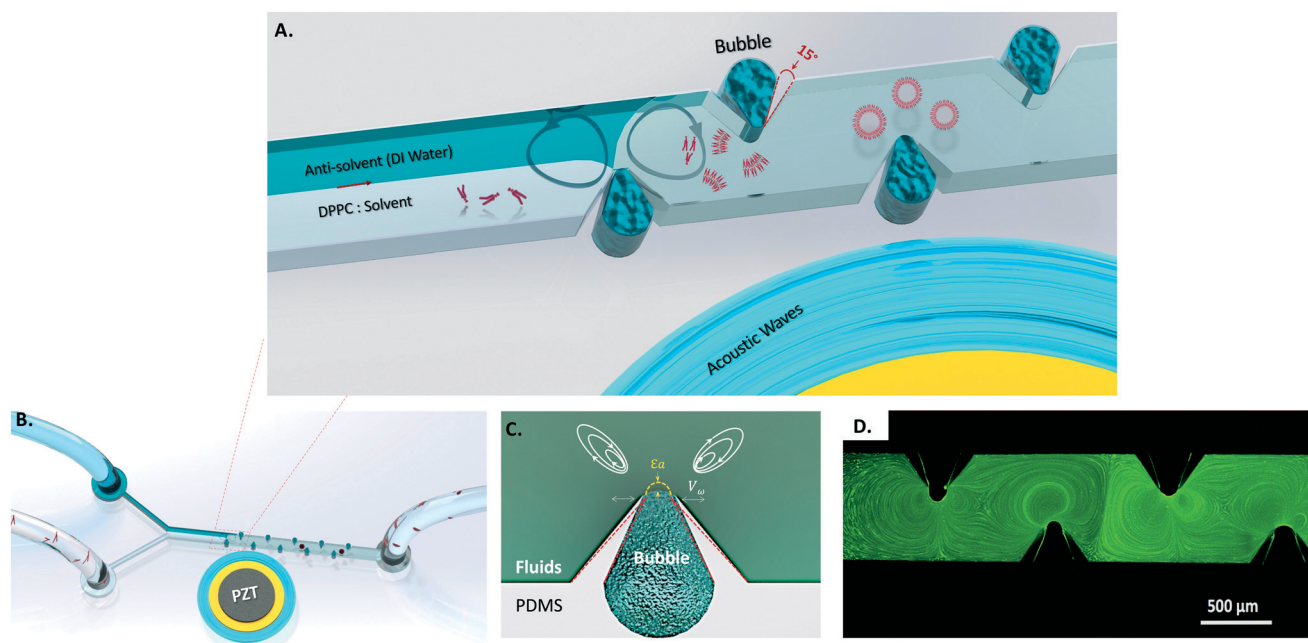

Fig. 1 A) Conceptual illustration of the acoustic streaming and the resultant mixing used for self-assembly of nanoparticles. B) Rendered picture of the acoustic platform. The piezoelectric transducer is embedded next to the PDMS part, emitting acoustic pressure waves. C) Schematic drawing of the combined unit. Slanted sharp edges allow a bubble to be trapped. D) Fluorescent polystyrene particle (2 micron diameter) behavior in the presence of an acoustic field. The closed-circular pathline of microparticles shows complete coverage of the channel width.

amplitude of the voltage and transmit the signal to the piezoelectric transducer. The piezo element polarizes in the Z-direction in a synchronized response to the electric excitation; however, the oscillation occurs in all directions owing to both direct and transverse effects.[42] The electrical impedance of the transducer system was measured with an Agilent 4294A impedance analyzer (Agilent, Palo Alto, CA). The spectra of 40 Hz–100 kHz were explored using 201 nodes. The piezo elements were mounted on the chip and connected to low and high voltage terminals with a peak-to-peak amplitude of 1 V_{pp}.

Nanoparticle synthesis and characterization

The mixtures of precursor monomers in the organic solvent were prepared by dissolving various concentrations of PLGA-PEG in 50% acetonitrile : 50% DMSO for polymeric nanoparticles and DPPC : cholesterol in 70% IPA for liposome generation. Ultrapure water was collected from a Barnstead Nanopure filtration system with a resistivity above 18.2 MΩ cm. The organic solution and DI water were infused with a Harvard syringe pump with a flow rate ratio of 1 : 4 for polymeric nanoparticles and 1 : 6 for liposomes. PTFE tubing was used to deliver the solutions to the channels. The hydrodynamic diameter, distribution by volume, and polydispersity index (PDI) of the PLGA-PEG nanoparticles were measured by dynamic light scattering (DLS) using a ZetaPALS zeta potential analyzer (Brookhaven Instruments Corp., USA). Nanoparticle tracking analysis (NTA) was conducted to measure the concentration of the synthesized nanoparticles using a NanoSight 300 (NanoSight, Amesbury, United Kingdom) with a 640 nm laser at $T = 25$ °C. Measurements were performed in dynamic flow mode controlled with a built in syringe pump at level 60. The TEM (transmission electron microscopy) images of the PLGA-PEG nanoparticles and liposomes were acquired after negative staining with 2% solution of uranyl acetate with a Tecnai 12 BioTwin electron microscope, FEITechnologies Inc., USA at an acceleration voltage of 120 kV.

Results and discussion

The variation of pressure and the velocity field caused by acoustic effects generates streams around the sharp-edge and bubble structure. To verify this effect in our platform and picture the formed flow pattern, a solution of DI water and fluorescently labeled polystyrene beads with 2 micrometer diameter was infused into the microchannels. Small fluorescent particles lend themselves to minimizing the acoustic radiation force,[43] pointing the spotlight on the microstreaming effect. In the absence of a background flow and acoustic streaming, the particles remain quiescent. By introducing an acoustic field upon activation of the piezoelectric transducer, the microparticles start to circulate in closed trajectories which help to visualize the pattern of the vortices (Video S2†). To spot the most pronounced microstreams, the transducer excitation frequency was increased in 100 Hz steps from 1

kHz to 150 kHz, while visually exploring for distinguished prevalence of the acoustic vortices. The microstreams were observable on multiple frequencies, but the effect was prominent at a frequency of 74.2 kHz. Fig. 1D illustrates the pathline pattern of the acoustic microstream at this frequency through the trajectories of the fluorescent microparticles. The closed pattern of the streamlines affirms that their origin is the hydrodynamic forces of the microstreams rather than the acoustic radiation forces on the microparticles. This verifies the trajectories as a pertinent representative of the flow field.[20]

Comparing the microstream patterns of sharp edges, bubbles, and the combined unit

To fathom the impact of bubbles, half of the channel was treated with ethanol, which has a low surface tension, to prevent the bubble trapping. Ethanol was then withdrawn and replaced by a suspension of microparticles. As a result, the bubbles could only be trapped in the unexposed half of the channel. The frequency exploration was performed to find the resonance frequency for structures without a bubble. Interestingly, their prominent microstreams were generated at 74.2 kHz, which was the same as the frequency of the structure with a bubble. The intensity of the microstreams, however, showed a significant difference. Fig. 2A and Video S3† present the difference in the acoustic microstream intensity in the same device for two sharp edges, with and without a bubble in their vicinity. As can be perceived in the left portion of the microfluidic device (no bubble), the microstreams are substantially weaker than those of the structure with a bubble. To investigate the contribution of sharp edges to the microstreaming, the sharp edges were replaced by non-sharp bars of the same size and with increasing distances to trap air bubbles of different sizes ($r_e \approx 65$–100 μm). Fig. 2B shows the microstreaming intensity for bubbles in the absence of sharp edges (Video S4† shows the streams). The produced microstreams had a comparable intensity to those of sharp edges without a bubble (Fig. 2A left) but were considerably weaker than the microstreams formed by the combined unit (Fig. 2A right). Another interesting observation is that the microstreams of both bars at the sides were stronger than the ones in the middle. This can be due to the addition of vibration of bars, even though they are not sharp, to the microstreaming effect.

The mixing capacity in each design was assessed by evaluating the mixing quality through the width of the channel. Although the definition of sufficient mixing is subjective to the specific application, a mixing index of 80% is commonly considered as an adequate mixing[30,31] and therefore is designated as the lower threshold in this study (details of MI calculation in the ESI†). Fig. 2C shows the significant advantage of the combined design over bubbles and sharp edges alone in the allowable throughput that can reach the adequate mixing. It can be perceived that the effect is more than the simple superposition of sharp-edge and
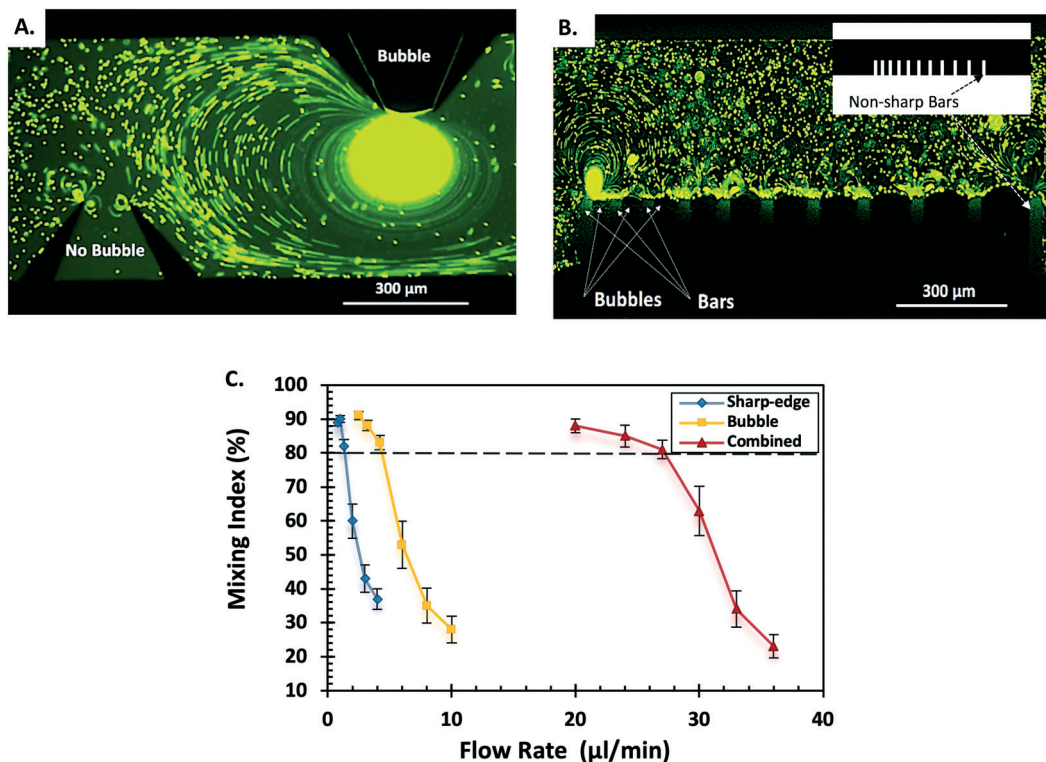
Fig. 2 A) Microstreaming comparison with and without bubbles. The left structure is filled with the particle solution and shows limited streaming of the sharp edge structure while the combined unit on the right of the picture with bubbles ($r_e \approx 98$ μm) induces strong microstreams which span through the channel width. B) The microstreaming pattern of the bubbles of different sizes ($r_e \approx 65$–100 μm) which are trapped between PDMS bars in the absence of sharp edges. The microstream intensity is comparable to that of the sharp edges without bubbles and considerably weaker than that of the combined unit. C) Characterization of mixing performance and allowable throughput to reach the mixing threshold (MI = 80%) in each of the designs at an excitation voltage of 15 V_{pp}.

bubble microstreams. This implies that the integration of sharp edges and bubbles can have a synergistic effect on each other in that the presence of a bubble can facilitate vibration of the sharp edge by (a) amplifying and focusing the acoustic field in its vicinity[40] and (b) reducing the viscous resistance to the vibrational motion due to the significantly lower viscosity of air compared to liquids.[40] The vibration of sharp edges can reciprocally contribute to the bubble's volumetric pulsation by varying their intermediate space. The existence of these two features in the proximity of each other can create a positive feedback loop which exponentially boosts the produced microstreams. This obviates the need for high voltages to reach effective mixing, and thus, lowers the input energy and the subsequent heating effect that can be detrimental to many biological applications.

Mixing assessment

Uniform mixing requires prevalence of the motion momentum of acoustic microstreams over the laminar flow to disrupt its parallel streamlines, including the interface of fluids. For zones of the channel not exposed to the microstreams, the background flow preserves its parallel streamlines, limiting mass transport to inefficient diffusion. Hence, the competition between the acoustic microstream

and the background flow to conquer the flow field determines the quality of mixing. Stronger microstreams can expand through the channel and disrupt all streamlines while a stronger background flow can suppress microstreams and confine their effect. Apart from the intrinsic behavior of the oscillatory structures (bubbles and edges), three factors are at play in this competition: the optimum frequency that emanates the maximum driving pressure, the input voltage which controls the driving pressure, and the flow rate of the background flow which tends to suppress the microstream. These three criteria are examined for the proposed micromixer to determine the impact of each of them on the mixing performance of the system.

Effect of frequency on mixing performance

The resonance of bubbles and the piezoelectric transducer are both known to influence the intensity of acoustic streaming. However, the optimum frequency is attributed to the resonance frequency of one or another in different studies. Locating the optimum frequency is usually done by visual observation of pronounced microstreams as described earlier. To quantitatively analyze the relationship between the frequency and microstream intensity as well as to identify the nature of the dominant resonance in this platform, different

types of piezo elements were used and the electrical impedance values of each and their corresponding mixing indices within the range of 40 Hz–100 kHz were measured. Three models of piezo elements from RadioShack, STEMINC, and Thorlabs with dissimilar natural frequencies were embedded adjacent to the identical channel geometry and were resonated with 10 V_{pp}. Fig. 3 shows the impedance value of each piezo element and the outcome mixing index as a function of frequency. The local extrema nodes in the graphs from the impedance analyzer indicate the vibrational resonance frequency of the mounted piezo element. Given that the mechanical impedance is the lowest at the resonance frequency, the vibration amplitude and the resultant acoustic pressure show the highest local amplitude at the resonance frequency node.[42,44] The mixing indices reached their maximum value at the proximity of the resonance frequency of each piezoelectric transducer system, while at the resonance frequency of the bubble, which was calculated to be 33.7 kHz by the Rayleigh–Plesset equation,[45] the MI did not show significant fluctuations. For the rest of the experiments, the frequency was set at its optimal value to gain the maximum driving pressure from the piezo elements.

Effect of voltage on mixing performance

As shown in eqn (3), the velocity of the microstreams is proportional to the square of the oscillation amplitude.[28] An influential parameter in the oscillation amplitude is the input voltage of the driving signal, which has a square relationship with electrical power.[31] Fig. S5 and Video S5† show the concentration distribution of fluorescein for different input voltages at a constant flow rate and frequency. At 10 V_{pp}, the mixing distance to reach the threshold of adequate mixing (MI = 80%) is approximately 2500 μm. As the input electrical power is amplified, the acoustic wave power emitted by the transducer increases. This leads to a higher vibration amplitude and stronger fluid motion as observed in Fig. 4A. Strong microstreams are generated instantaneously and homogeneous mixing occurs at 14 V_{pp}. Increasing the voltages over 14 V_{pp} does not alter the mixing pattern significantly, rendering this

voltage the optimum for a flow rate of 18 μL min^{-1}. The mixing length for this condition, which is the shortest one, was measured by calculating the thickness of transition from the unmixed zone with a normalized concentration of ≈1 (dark side) to 0.6 which corresponds to 80% mixing. The thickness was measured for ten positions on the transition line and found to be in the range of 25.2 ± 2.3 μm (Fig. 4B).

Effect of the flow rate on mixing performance

To investigate the impact of the flow rate on the mixing index, the signal's voltage was kept constant at 10 V_{pp} and the flow rate was altered. Fig. S6 and Video S6† show the mixing performance with flow rates of 12 μL min^{-1} to 24 μL min^{-1}. For the experiment with the flow rate of 12 μL min^{-1}, the mixing index reached its threshold within 25.2 ± 2.3 μm. As the flow rate increased, the background field became stronger and started to suppress the acoustic microstream and narrowed its domain of motion. In contrast, the flow rate of 24 μL min^{-1} predominantly overpowered the microstream and dropped the mixing index. The balance between the driving voltage and the flow rate is key to both optimizing the energy consumption and controlling the mixing time. Time is an important factor in mixing and can be determined by $t_{mix} = L_{mix}/V$ where t_{mix} shows the time of mixing, L_{mix} is the distance required for the fluid to reach the mixing threshold, and V is the net velocity of fluids in the channel direction. Fig. 4C shows the balance of the input voltage and the flow rate for reaching the mixing threshold at the mixing length of 25.2 μm. The graph shows a linear relationship on the logarithmic scale between the flow rate and the input voltage with a slope of 1.75. This is in line with the linear relationship (on the logarithmic scale with a slope of 2) between the electrical power and the voltage which transduces to mechanical vibration and finally, fluid streams. The difference in the slopes can be attributed to the damping effect. One can use this diagram for alternating voltage or the flow rate to adjust the time of mixing while having a satisfactory mixing index. For applications requiring extremely fast mixing, such as nanoparticle synthesis, voltages should be
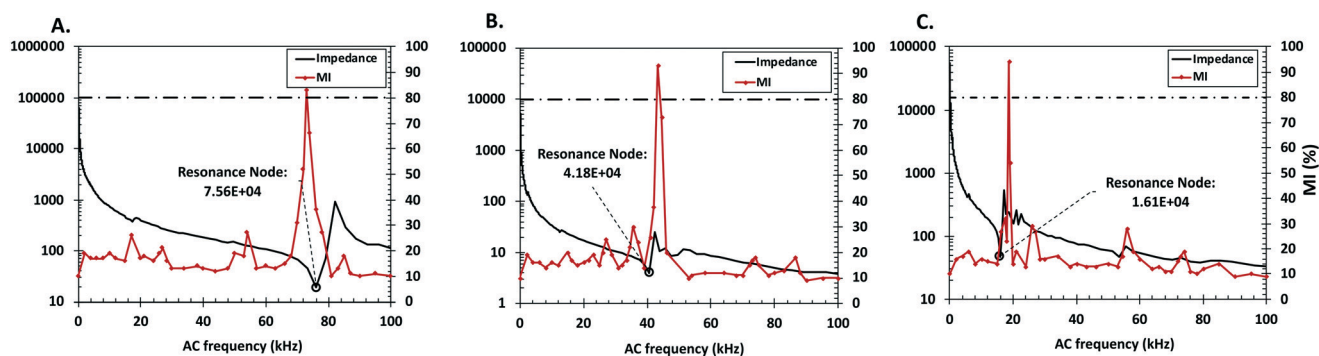

Fig. 3 Sonograms of three piezoelectric transducers from A) RadioShack, B) Thorlabs and C) STEMINC and the mixing indices (MIs) for their corresponding platforms. For each piezoelectric system, the highest mixing index appears at the proximity of its resonance frequency, confirming the dominant effect of electromechanical resonance (the mixing index is average of two repetitions).
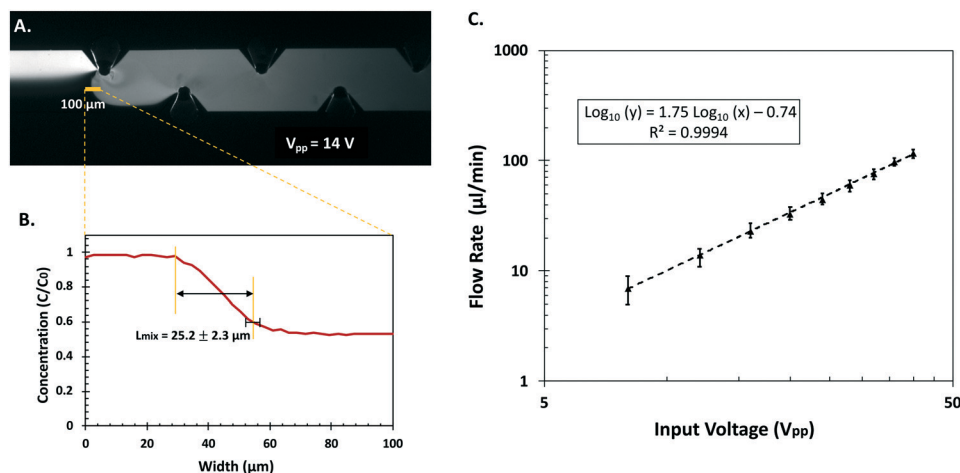
Fig. 4 A) The mixing performance in the presence of acoustic mixing at an input voltage of 14 V_{pp} and a flow rate of 18 μL min^{-1}. B) The minimum length required to reach the adequate mixing threshold (normalized concentration of 0.6, *i.e.* MI = 0.8). C) The relationship between the input voltage and flow rate to reach the adequate mixing threshold in the designated mixing length (25.2 μm).
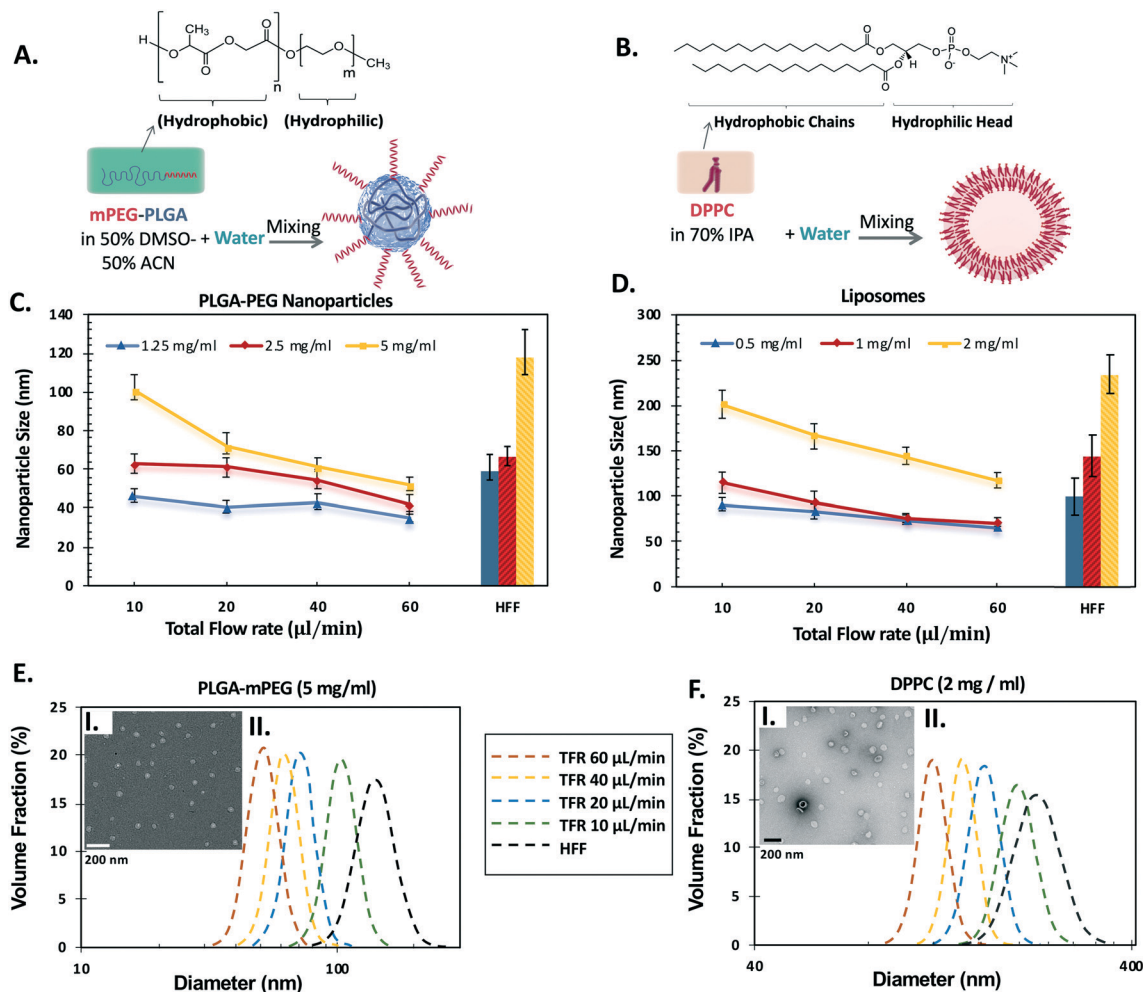

Fig. 5 A) Schematic of PLGA-PEG nanoparticle synthesis. B) Schematic of liposome synthesis. Size variation of C) PLGA-PEG nanoparticles and D) liposomes synthesized in the acoustic platform by changing the mixing time through the total flow rate and comparison with the hydrodynamic flow focusing method for three different concentrations of precursors. E) I. TEM image of PLGA-PEG nanoparticles. II. Size and size distribution as measured by DLS. F) I. TEM image of nanoliposomes by negative staining. II. Size and size distribution as measured by DLS.

equal or higher than the balance diagram to ensure the shortest mixing length. The fastest mixing time of 0.8 ms was obtained within this mixing length for a flow rate of 116 μL min^{-1} at an input voltage of 40 V$_{pp}$.

Nanoparticle synthesis

For the proof of concept, the micromixer platform was employed as a synthesis unit to control the nanoprecipitation process by regulating the mixing time and homogenizing the nucleation environment. The entire microchannels were coated with Parylene-C dimers through chemical vapor deposition (CVD) to prevent the diffusion of uncross-linked PDMS oligomers to the synthesis unit and ensure the solvent compatibility of the device. To show the versatility of our device, liposomes as hollow nanoshells and rigid PLGA-PEG nanoparticles were synthesized. These two families of organic nanoparticles are extensively employed as FDA-approved controlled release systems in pharmaceutical and biomedical fields owing to their biocompatibility, biodegradability, and surface tunability.

Both liposome and PLGA-PEG nanoparticle generation processes started with dissolving the precursors in a water-miscible organic solvent (Fig. 5A and B). Upon contact of these solutions with co-flowing DI water (anti-solvent), the hydrophobic forces cause the precursors to self-assemble into nanoparticles in a thermodynamically-driven process. The hydrophilic component of the precursors (PEG in PLGA-PEG and phosphate head in phospholipids) forms a barrier on the surface of the nanoparticles to prevent further addition of precursors. When mixing is incomplete, this hydrophilic shield is not robust enough to block further aggregation, leading to the formation of larger NPs with higher polydispersity. The introduction of acoustic microstreams increases the interface and normal advection to mix solutions with antisolvent in a millisecond order. This rapid mixing ensures the homogeneous environment prior to nucleation and aggregation of amphiphilic precursors which is essential for the formation of a monodisperse population of nanoparticles.[46,47] Four important parameters, *i.e.* size, size distribution, the concentration of nanoparticles synthesized in the micromixer, and the level of aggregation, were used as the measures for the performance of the acoustic platform in making nanoparticles. Hydrodynamic flow focusing (HFF), commonly reported in the literature as a standard microfluidic nanoparticle synthesis method, was opted as the comparison reference.

1) Nanoparticle size tuning. Size is deemed to be one of the most decisive physicochemical characteristics of nanoparticles for their interactions with the reticuloendothelial system (RES), transcytosis pathways, the payload release rate and cellular uptake and renal clearance to name a few. The nanoparticle size is tightly dependent on the mixing time and nucleation homogeneity.[48,49] First, to examine the capability of the acoustic microfluidic platform to finely tune the nanoparticle size, the mixing time was varied by altering the

total flow rate (TFR) at a fixed voltage of 30 V$_{pp}$. Fig. 5C and D show the variation in the average diameter of nanoparticles, measured by dynamic light scattering (DLS), for total flow rates of 10 μL min^{-1}, 20 μL min^{-1}, 40 μL min^{-1}, and 60 μL min^{-1}, and the HFF method. Since the most influential factor on the size of nanoparticles produced in the HFF method is the flow rate ratio (FRR) of the precursor–solvent mixture and the antisolvent, therefore, it is kept constant for the HFF and acoustic experiments to be consistent in comparison. However, the mixing mechanism in the acoustic platform is not dependent on the FRR which means that the precursor–solvent flow rate should not be decreased to achieve adequate mixing. Therefore, the dilution of produced nanoparticles which is a common challenge in the HFF method can be addressed.

For all the flow rates, the nanoparticles were smaller in the acoustic micromixer compared to those in the HFF method which relies merely on slow diffusion. At the slowest flow rate, *i.e.* 10 μL min^{-1}, the size of nanoparticles was closest to that of HFF. This can also be due to the occurrence of some extent of diffusion before reaching the mixing units. As the total flow rate increased, the mixing time decreased proportionally and thereby led to smaller diameter nanoparticles. This trend was reproducible for three different concentrations of PLGA-PEG. For 1.25 mg ml^{-1}, the nanoparticle size could be tailored from 59.1 ± 11.3 nm offered by HFF to the minimum of 35.1 ± 6.2 nm, for 2.5 mg mL^{-1}, the range was between 67.6 ± 16.1 nm and 42.4 ± 7.2 nm, and for 5 mg ml^{-1}, the nanoparticle size could be tuned between the range of 118.9 ± 32.1 nm for HFF and 51.9 ± 6.8 nm for TFR = 60 μL min^{-1}. The larger size for higher concentrations was in line with Johnson's[50] study which stated that the time of aggregation decreases with the increase in the initial concentration. Thus, as the concentration increases, the gap between τ_{agg} and τ_{mix}, which is a window for the addition of dispersed precursors, increases and results in larger nanoparticles. It also explains the wider size distribution with the change in the mixing time in higher concentrations.

Liposome synthesis was also conducted with flow rates of 10 μL min^{-1}, 20 μL min^{-1}, 40 μL min^{-1}, and 60 μL min^{-1}. For the concentration of 0.5 mg ml^{-1}, the size of nanoparticles was modulated from 101.1 ± 17.4 nm with the HFF method to 65 ± 4.1 nm at the fastest TFR. For the concentration of 1 mg ml^{-1}, the size range was between 144.3 ± 15.6 nm and 70.9 ± 4.9 nm and for the concentration of 2 mg ml^{-1}, the size could be varied from 234.4 ± 17.1 nm to 117.5 ± 9.2 nm. The rate of change in size in response to the TFR also offers insight into analyzing the process. The decrease in size is steeper for the concentration of 2 mg ml^{-1} than 1 mg ml^{-1} and it is the least for 0.5 mg ml^{-1}. However, the rates of change decreased at a higher TFR, which showed a tendency to converge as the mixing accelerates. This is congruous with Johnson's[50] size-mixing time diagram that shows a minimum threshold limit for the size of nanoparticles.

2) Size distribution of nanoparticles. The polydispersity indices of nanoparticles were 0.072 for PLGA-PEG

nanoparticles and 0.125 for liposomes. Fig. 5E.I, and F.I show the TEM images of PLGA-PEG nanoparticles and liposomes synthesized using the acoustic mixer. These images confirmed the low polydispersity in the size distribution of the nanoparticles and the absence of large aggregation of precursors. The actual diameter of the nanoparticles, which is usually smaller than the hydrodynamic one, was also measured by processing the TEM image *via* ImageJ software. An average of 57.4 ± 5.2 nm and 73.1 ± 8.1 nm was found for PLGA-PEG nanoparticles and nanoliposomes, respectively. The DLS results of the size distribution for the nanoparticles synthesized with the acoustic platform and the HFF method with the above flow rates and concentrations are shown in Fig. 5E.II and F.II and S8.† As anticipated, the size distributions of the NPs from HFF were wider due to the slower nanoprecipitation. In the acoustic platform, as the mixing time decreased with the increase in the TFR, the nanoparticle size distributions tended towards narrower polydispersity. This trend was more discernable in liposome experiments.

3) **Concentration of nanoparticles and effect of aggregates.** The initial concentration of the precursors is often considered as the yield of the nanoparticle generation systems in the absence of an actual direct method for nanoparticle concentration measurement. Amrani *et al.*[15] were among the first to use the nanoparticle tracking analysis (NTA) to measure the concentration of liposomes at the output of an HFF system. Interestingly, the authors showed that not only an increase in precursor concentration does not necessarily translate to an increase in the number of nanoparticles, but also it could reduce the nanoparticle concentration at the output. Apart from the size difference, this discrepancy between the initial concentration and the number of nanoparticles at the output can be attributed to the formation of few but large aggregates, which is common in HFF methods.

To understand whether the intense acoustic microstream and rapid homogenization can alleviate the aggregation and influence the yield of nanoparticle formation, samples of liposomes synthesized with HFF and the acoustic device for three different precursor concentrations were measured with NTA. The results showed an increase in the produced liposomes in the acoustic method compared to those in the HFF method for each precursor concentration (Fig. 6). The pervasive acoustic microstreams across the channel increase the interface of the solvent–solute mixture and antisolvent where the formation starts, and by creating a homogeneous environment during self-assembly, it reduces the risk of formation of big aggregates. As a result, this method can be an efficient procedure of nanoparticle generation with a higher nanoparticle output compared to HFF at the same precursor concentration.

Conclusion

We introduced an ultra-rapid, efficient, and practical acoustically-driven microfluidic micromixer through integrating bubbles and sharp edges in the device. We demonstrated that
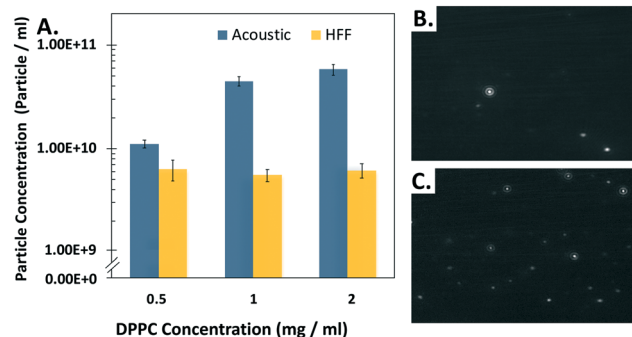

Fig. 6 A) Nanoliposome concentration synthesized in the acoustic and HFF platforms for three different concentrations of precursors. B) NTA video frame of liposomes produced in the HFF method with an average of 4.6 ± 0.4 particles per frame with a dilution factor of 200. C) NTA video frame of liposomes produced in the acoustic micromixer with an average of 23.3 ± 2.1 particles per frame with a dilution factor of 200.

these features act synergistically to maximize the conversion of the acoustic pressure to high-amplitude vibrations and produce considerably stronger and broader microstreams compared to the designs exhibiting only one of these features. The bubbles increase the sharp edge vibration by local amplification of the acoustic field and by reducing the viscous resistance to the vibrational motion. The sharp edges can also contribute to the bubble volume pulsation by varying their intermediate space. The acoustic microstreams showed the capacity for accelerating the mixing process to 0.8 ms at a flow rate of 116 μL min^{-1}, which is meaningfully faster than those of available acoustic micromixers in the literature. Due to the pronounced microstreaming effect, the mixing capacity of this design for the same input voltage is higher which can be an advantage in the setups with limited output voltage such as the emerging field of cell phone guided microfluidics.[51] The inherent high-controllability of the acoustic streams through governing the input electrical energy lent itself to a well-regulated mixing process necessary for uniform nanoprecipitation. This capability was used to synthesize monodispersed PLGA-PEG nanoparticles and nanoliposomes. Through alteration of the mixing time, the nucleation process of nanoparticles was manipulated to finely tune their size. This technique can be employed to reproducibly synthesize nanoparticles with the desired size for a specific application or to generate a library of organic nanoparticles with a broad range of physicochemical properties. The intense mixing allowed the production of a higher number of nanoparticles in the acoustic platform compared to that of the HFF method. Also, the intense and pervasive acoustic microstreams in this platform prevent the formation of large nanoparticle aggregates and clogging of the channel, which is a common challenge in microfluidic platforms.

Conflicts of interest

There are no conflicts of interests.

Acknowledgements

References

1 C. Vauthier and G. Ponchel, *Polymer Nanoparticles for Nanomedicines*, Springer, 2017.

2 Y. Kim, B. Lee Chung, M. Ma, W. J. Mulder, Z. A. Fayad, O. C. Farokhzad and R. Langer, *Nano Lett.*, 2012, **12**, 3587–3591.

3 P. M. Valencia, O. C. Farokhzad, R. Karnik and R. Langer, *Nat. Nanotechnol.*, 2012, 7, 623.

4 Z. Mahmoodi, J. Mohammadnejad, S. R. Bazaz, A. A. Mehrizi, M. A. Ghiass, M. Saidijam, R. Dinarvand, M. E. Warkiani and M. Soleimani, *Drug Delivery Transl. Res.*, 2019, **9**, 707–720.

5 L. Zhang, Q. Feng, J. Wang, S. Zhang, B. Ding, Y. Wei, M. Dong, J.-Y. Ryu, T.-Y. Yoon and X. Shi, *et al.*, *ACS Nano*, 2015, **9**, 9912–9921.

6 C. J. M. Rivas, M. Tarhini, W. Badri, K. Miladi, H. Greige-Gerges, Q. A. Nazari, S. A. G. Rodríguez, R. Á. Román, H. Fessi and A. Elaissari, *Int. J. Pharm.*, 2017, **532**, 66–81.

7 R. Tanaka, N. Takahashi, Y. Nakamura, Y. Hattori, K. Ashizawa and M. Otsuka, *RSC Adv.*, 2016, **6**, 87049–87057.

8 G. Cai, L. Xue, H. Zhang and J. Lin, *Micromachines*, 2017, **8**, 274.

9 J. B. Knight, A. Vishwanath, J. P. Brody and R. H. Austin, *Phys. Rev. Lett.*, 1998, **80**, 3863.

10 A. Lashkaripour, C. Rodriguez, L. Ortiz and D. Densmore, *Lab Chip*, 2019, **19**, 1041–1053.

11 A. D. Stroock, S. K. Dertinger, A. Ajdari, I. Mezić, H. A. Stone and G. M. Whitesides, *Science*, 2002, **295**, 647–651.

12 M. Rasouli, A. A. Mehrizi, M. Goharimanesh, A. Lashkaripour and S. R. Bazaz, *Chem. Eng. Process.*, 2018, **132**, 175–186.

13 C.-Y. Lee, W.-T. Wang, C.-C. Liu and L.-M. Fu, *Chem. Eng. J.*, 2016, **288**, 146–160.

14 N. M. Belliveau, J. Huft, P. J. Lin, S. Chen, A. K. Leung, T. J. Leaver, A. W. Wild, J. B. Lee, R. J. Taylor and Y. K. Tam, *et al.*, *Mol. Ther.–Nucleic Acids*, 2012, **1**, e37.

15 S. Amrani and M. Tabrizian, *ACS Biomater. Sci. Eng.*, 2018, **4**, 502–513.

16 D. Carugo, E. Bottaro, J. Owen, E. Stride and C. Nastruzzi, *Sci. Rep.*, 2016, **6**, 25876.

17 S. Wang, X. Huang and C. Yang, *Lab Chip*, 2011, **11**, 2081–2087.

18 A. Bernassau, P. Glynne-Jones, F. Gesellchen, M. Riehle, M. Hill and D. Cumming, *Ultrasonics*, 2014, **54**, 268–274.

19 D. J. Collins, Z. Ma and Y. Ai, *Anal. Chem.*, 2016, **88**, 5513–5522.

20 I. Leibacher, P. Hahn and J. Dual, *Microfluid. Nanofluid.*, 2015, **19**, 923–933.

21 A. Hashmi, G. Yu, M. Reilly-Collette, G. Heiman and J. Xu, *Lab Chip*, 2012, **12**, 4216–4227.

22 C. Wang, B. Rallabandi and S. Hilgenfeldt, *Phys. Fluids*, 2013, **25**, 022002.

23 L. Capretto, W. Cheng, M. Hill and X. Zhang, *Microfluidics*, Springer, 2011, pp. 27–68.

24 R. H. Liu, J. Yang, M. Z. Pindera, M. Athavale and P. Grodzinski, *Lab Chip*, 2002, **2**, 151–157.

25 D. Ahmed, C. Y. Chan, S.-C. S. Lin, H. S. Muddana, N. Nama, S. J. Benkovic and T. J. Huang, *Lab Chip*, 2013, **13**, 328–331.

26 R. H. Liu, R. Lenigk, R. L. Druyor-Sanchez, J. Yang and P. Grodzinski, *Anal. Chem.*, 2003, **75**, 1911–1917.

27 Y. Xie, D. Ahmed, M. I. Lapsley, S.-C. S. Lin, A. A. Nawaz, L. Wang and T. J. Huang, *Anal. Chem.*, 2012, **84**, 7495–7501.

28 M. V. Patel, I. A. Nanayakkara, M. G. Simon and A. P. Lee, *Lab Chip*, 2014, **14**, 3860–3872.

29 S. Yazdi and A. M. Ardekani, *Biomicrofluidics*, 2012, **6**, 044114.

30 N. Nama, P.-H. Huang, T. J. Huang and F. Costanzo, *Lab Chip*, 2014, **14**, 2824–2836.

31 P.-H. Huang, Y. Xie, D. Ahmed, J. Rufo, N. Nama, Y. Chen, C. Y. Chan and T. J. Huang, *Lab Chip*, 2013, **13**, 3847–3852.

32 R. Green, M. Ohlin and M. Wiklund, Applications of acoustic streaming in microfluidic devices, *Microscale Acoustofluidics*, 2014, ch. 13, pp. 312–336.

33 J. Lei, P. Glynne-Jones and M. Hill, *Microfluid. Nanofluid.*, 2017, **21**, 23.

34 J. W. S. B. Rayleigh, *Scientific papers*, University Press, 1899, vol. 1.

35 L. Rayleigh, *Proc. R. Soc. London*, 1883, **36**, 10–11.

36 J. Stuart, *Clarendon*, Oxford, 1963.

37 L. Zarembo, *High-intensity ultrasonic fields*, Springer, 1971, pp. 135–199.

38 R. Manasseh, *Handbook of Ultrasonics and Sonochemistry*, 2016, 1–36.

39 S. A. Elder, *J. Acoust. Soc. Am.*, 1959, **31**, 54–64.

40 T. Leighton, *Ultrason. Sonochem.*, 1995, **2**, S123–S136.

41 M. Ovchinnikov, J. Zhou and S. Yalamanchili, *J. Acoust. Soc. Am.*, 2014, **136**, 22–29.

42 J. L. Pons, *Emerging actuator technologies: a micromechatronic approach*, John Wiley & Sons, 2005.

43 A. Lenshof, C. Magnusson and T. Laurell, *Lab Chip*, 2012, **12**, 1210–1223.

44 S. S. Rao and F. F. Yap, *Mechanical vibrations*, Prentice Hall Upper Saddle River, 2011, vol. 4.

45 D. Ahmed, X. Mao, J. Shi, B. K. Juluri and T. J. Huang, *Lab Chip*, 2009, **9**, 2738–2741.

46 L. Capretto, D. Carugo, S. Mazzitelli, C. Nastruzzi and X. Zhang, *Adv. Drug Delivery Rev.*, 2013, **65**, 1496–1532.

47 S. Ding, N. Anton, T. F. Vandamme and C. A. Serra, *Expert Opin. Drug Delivery*, 2016, **13**, 1447–1460.

48 S. Chopra, N. Bertrand, J.-M. Lim, A. Wang, O. C. Farokhzad and R. Karnik, *ACS Appl. Mater. Interfaces*, 2017, **9**, 11440–11450.

49 D. Liu, H. Zhang, F. Fontana, J. T. Hirvonen and H. A. Santos, *Lab Chip*, 2017, **17**, 1856–1883.

50 B. K. Johnson and R. K. Prud'homme, *Phys. Rev. Lett.*, 2003, **91**, 118302.

51 H. Bachman, P.-H. Huang, S. Zhao, S. Yang, P. Zhang, H. Fu and T. J. Huang, *Lab Chip*, 2018, **18**, 433–441.